



Pushing the boundaries
of chemistry?
It takes
#HumanChemistry

Make your curiosity and talent as a chemist matter to the world with a specialty chemicals leader. Together, we combine cutting-edge science with engineering expertise to create solutions that answer real-world problems. Find out how our approach to technology creates more opportunities for growth, and see what chemistry can do for you at:

[evonik.com/career](https://www.evonik.com/career)



Microstructural, Mechanical, and Tribological Evolution under Different Heat Treatment Conditions of Inconel 625 Alloy Fabricated by Selective Laser Melting

Riccardo Ferraresi,* Andrea Avanzini, Silvia Cecchel, Candida Petrogalli, and Giovanna Cornacchia*

Additive manufacturing (AM) can be particularly advantageous to manufacture components designed to meet challenging structural requirements. Selective laser melting (SLM) microstructure is different than that obtained by traditional manufacturing process; in particular, mechanical and microstructural features achieved herein are influenced by the entire thermal history, including the manufacturing process and the heat treatment (HT) with relevant role of the slow cooling rate adopted. In fact, both the process and the HTs can significantly modify the microstructure and related mechanical and tribological properties. To better understand how mechanical response can be tuned to meet different requirements, in this article the effects of four different vacuum HTs on microstructures, mechanical properties, and wear behavior of Inconel 625 produced with SLM are deeply investigated. In general, the results confirm that HT can significantly change the microstructure and mechanical or tribological properties of Inconel 625. Among the examined HT, solution + aging and direct aging improve the strength of the alloy, whereas annealing leads to recrystallization, reducing strength in favor of ductility. Stress relieving does not significantly change the microstructure and mechanical properties. Considering tribological behavior, only direct aging HT leads to a remarkable improvement, with a reduction in friction coefficient and wear rate.

mechanical strength, durability, and wear, associated with corrosion resistance and fatigue life in a wide range of temperatures, from cryogenic conditions up to 982 °C.^[1] IN625 has excellent chemical resistance in different aggressive environments and temperatures range, as well as high creep strength and weldability. Thanks to these properties, IN625 is extensively used in different fields such as aerospace, chemical, petrochemical, and marine industries.^[1]

In recent times, greater attention has been directed to the use of additive manufacturing (AM) technique for the production of IN625 components for the energy sector,^[2,3] such as gas turbine blades, heat exchangers, and parts for chemical reactors.^[1] This increasing interest is directly related to the need of producing innovative components with complex shapes, as those resulting from topological optimization, to maximize the performance-on-weight ratio and, consequently, the efficiency. For this purpose, one of the most used AM techniques is selective


laser melting (SLM), which belongs to the broader family of laser powder bed fusion (L-PBF) technologies. Although the SLM process offers great advantages when manufacturing complex parts with high material utilization rate, the properties obtained are affected by many factors, like the characteristics of the printer hardware, the powder feedstock, and the choice of printing parameters (i.e., laser energy input and scan speed, scan strategy). On the one hand, the combination of these process-related factors may result in various types of defects such as gas or shrinkage porosity, cracks, lack of fusion or incomplete fusion holes, and impurities.^[4,5] For this reason, in the literature, there are several works concerning the optimization of the process parameters and scan strategy in order to obtain components with minimized defects.^[4–10]

On the other hand, the abovementioned factors also contribute to the way the physics of SLM processes evolves in terms of melting and solidification of material and related microstructural changes. In fact, an important aspect of SLM process is that the microstructure is usually different than the one observed in corresponding alloys produced with traditional methods, such as casting or forging.^[5] In general, as a result of SLM process, the as-built (AB)

1. Introduction

Inconel 625 (IN625) is a nickel-based superalloy with high chromium content that offers remarkable properties in terms of

R. Ferraresi, A. Avanzini, C. Petrogalli, G. Cornacchia
Department of Mechanical and Industrial Engineering
University of Brescia
via Branze 38, 25123 Brescia, Italy
E-mail: riccardo.ferraresi@unibs.it; giovanna.cornacchia@unibs.it
S. Cecchel
Research and Development
Streparava S.p.A.
Via Zocco 13, 25030 Adro (BS), Italy

 The ORCID identification number(s) for the author(s) of this article can be found under <https://doi.org/10.1002/adem.202100966>.

© 2021 The Authors. Advanced Engineering Materials published by Wiley-VCH GmbH. This is an open access article under the terms of the Creative Commons Attribution License, which permits use, distribution and reproduction in any medium, provided the original work is properly cited.

DOI: 10.1002/adem.202100966

microstructure is characterized by a regular distribution of overlapped melt pools, with columnar grains that grow in the build direction and are formed by a very fine dendritic structure. These columnar grains have a width of $\approx 25 \mu\text{m}$ and a length up to $400 \mu\text{m}$ ^[11] and their peculiar microstructure is mainly caused by the highly localized melting process, with a very rapid cooling rate ($\approx 10^6 \text{ K s}^{-1}$ ^[12,13]). The main thermal characteristics that control the solidification structure of an SLM product are the cooling rate, thermal gradient, and solidification rate at the solid–liquid interface. These parameters may influence microstructural features such as phase selection, microstructural length scales, and the transition from columnar to equiaxed growth.^[14] In particular, for SLM-IN625 the combination of high cooling rate and the thermal gradients suppresses the formation of secondary arms in the dendrites and can produce an alteration in the dendritic structure promoting the formation of a cellular structure.^[15,16]

Microstructural changes affect mechanical behavior and represent the underlying motivation of the different properties of SLM alloys when compared with wrought counterparts obtained with forging or casting. In the specific case of SLM-IN625, the values of hardness, yield strength, and ultimate tensile strength of the AB condition reported in the literature are generally higher than conventional methods whereas, on the contrary, the ductility decreases.^[16]

In this regard, heat treatment (HT) is certainly an effective way to tune mechanical properties as a function of the different requirements that a specific target component may impose. The main HTs performed on IN625 can be divided into four categories: stress relieving (SR), solution annealing (AN), direct aging (DA), and solution + aging (S + A) treatments.^[11–13,17–29] HTs are usually carried out in furnaces with a controlled atmosphere, and to the best of authors' knowledge, current literature is referred to this condition. Marchese et al.^[12] analyzed the effect of the AN temperatures on L-PBF IN625 specimens. The research demonstrated that complete recrystallization is achieved only above $1150 \text{ }^\circ\text{C}$, even if some equiaxed grains were visible at a temperature of about $1080 \text{ }^\circ\text{C}$. On the contrary, with the treatment at $870 \text{ }^\circ\text{C}$ it was possible to obtain only a SR. In terms of mechanical properties, the ultimate tensile strength (UTS) and the yield strength (YS) tended to decrease with the increase of the AN temperature. The opposite situation was observed for the elongation at break in fact; the ductility increased with increasing AN temperature. The progressive reduction of the mechanical properties and anisotropy was interpreted as consequences of the progressive recrystallization of the microstructure with the increase of the AN temperature. Similar conclusions about the effect of AN temperature on microstructure and mechanical properties can be found in other works.^[17–19] Li et al.^[18] and Li et al.^[19] also reported that increasing the AN temperature caused a microhardness reduction.

Xu et al.^[20] studied the effect of the aging treatment with or without a solution HT. In both cases, an increase of the mechanical properties (UTS and YS), thanks to the precipitation of reinforcing phases such as γ'' phase (Ni₃Nb) and carbides, was reached. The main effect of the solution HT before aging consisted in a more complete dissolution of the alloying elements, phases, and segregated zones that allowed to obtain an increased formation of precipitates. In addition, partial or complete recrystallization could be achieved, with isotropic behavior for both microstructure and mechanical properties. Marchese et al.^[21]

conducted an extensive study on the effects of temperatures and holding times of solutioning, DA, and solutioning with subsequent aging HTs. The DA treatment did not modify the microstructure which remained similar to the AB condition; the only difference observed consisted in the different types and number of precipitates. In fact, the aging treatment encouraged the formation of Cr-rich M₂₃C₆ carbides and strengthening phases such as γ'' . These precipitates can explain the highest tensile strength features, the lower ductility, and the presence of brittle fracture for this condition. As a result of solutioning treatment at $1150 \text{ }^\circ\text{C}$ complete recrystallization of the microstructure was observed, with a dissolution of the dendrites. This condition obviously led to a reduction in UTS and YS, but allowed reaching the best elongation at break among the different treatments considered, with a ductile fracture mode. The best combination of strength and ductility was achieved by solutioning with subsequent aging treatment that allowed to obtain a recrystallized microstructure together with strengthening precipitates (γ'' phase and Cr-rich M₂₃C₆ carbides). The fracture mode was a mix of brittle and ductile fracture. Another important posttreatment for the AM components is the hot isostatic pressing (HIP) studied, among other HTs, by Kreitzberg et al.^[29] Thanks to the high pressure applied on the component by an inert gas at high temperature, HIP HT is used to reduce typical AM defects, such as micro- and macroporosities, and to encourage the formation of a more isotropic microstructure. On the other hand, HIP treatment causes grain coarsening which is detrimental for the mechanical properties (except ductility^[29]). In fact, in the cited work, the mechanical properties of the HIP specimens were lower than other HTs (stress relief AN, recrystallization AN, and solution treatment), but with a greater elongation at break.

Due to the wide range of applications of IN625, it is also of fundamental importance to study its tribological behavior, but this aspect is much less investigated. Even considering IN625 manufactured with conventional routes, in the literature there are only a few works regarding wear or friction. Wang et al.^[30] investigated the wear resistance of extruded IN625 specimens using a ball-on-disk test at different temperatures (25, 250, and $500 \text{ }^\circ\text{C}$) and sliding speeds. Two different materials were used as counterparts: Si₃N₄ and GCr15. For both antagonist materials the friction coefficient increased with increasing temperature, but the friction coefficient with GCr15 was higher than that with Si₃N₄ at any temperature. It is important to highlight that the friction coefficient decreased with the increase of the sliding speed at any tested temperature. The same trend of the friction coefficient was reported for the specific wear rate, even if the maximum value of the latter was reached at the intermediate temperature of $250 \text{ }^\circ\text{C}$. As regards wear mechanisms, the adhesive one was observed for all temperature conditions tested when using GCr15 as counterpart although at high temperatures fatigue wear mechanism was also present. With Si₃N₄ counterpart, both adhesive and abrasive wear mechanisms were observed.

Deng et al.^[31] and Feng et al.^[32] studied instead the use of IN625 as a coating obtained by laser cladding technique. In particular, they investigated the wear behavior at high temperatures (550 , 600 , and $650 \text{ }^\circ\text{C}$) considering the evolution of the friction coefficient as a function of the time. In both works, increasing the temperature led to a reduction of the friction coefficient as well as of fluctuations over time and duration of run-in step.

Considering AM technologies, Tascioglu et al.^[33] investigated the effect of surface quality after a finish-milling operation on the wear resistance of SLM IN625. In particular, they studied three different values of cutting parameter: 0.05, 0.1, and 0.15 mm as feed per tooth. The wear resistance was evaluated by means of a linear reciprocating wear test using a tungsten carbide ball. They found that the Vickers microhardness remarkably increased in comparison with AB condition as a result of post-processing operation. This result was attributed to the presence of residual stress and an increase of dislocations because of plastic deformation due to the machining operation. A relationship between the feed rate and hardness was also established, with higher feed rates leading to higher hardness. In turn, this increased hardness directly affected the wear rate, with a reduction up to 50% compared with AB condition through finish-milling operations. Yong et al.^[34] studied the fretting wear resistance in a flat-on-flat configuration on SLM-IN625 superalloy. In this case, 42CrMo4 steel was used as antagonist material with different loads to evaluate the wear volume loss, the friction coefficient, and the width and the depth of the wear tracks. According to the authors, the wear volume loss and the depth of the track were very low and lower than traditionally manufactured IN625 specimens. The main wear mechanisms were tribo-oxidation and abrasive wear, mainly due to the formation of an oxide layer that can either protect the substrate or shatter in small fragments.

Basing on this brief review, it is clear that HT can profoundly affect the metallurgical, tribological, and mechanical performances of SLM-IN625, but a complete overview of their effects is still missing. Concerning the influence of HT on the mechanical properties of SLM-IN625, many themes have yet to be examined in depth, such as the effect of different HTs on the achievable range of mechanical properties or the possibility to balance contrasting requirements as a function of expected application.

In particular, while for this alloy different approaches to HT were proposed, previous investigations were limited to mechanical response, whereas a lack of data is observed, concerning the tribological behavior with the comparison of effects related to microstructural modifications induced by different HTs. In this sense, a further interesting option to be considered is provided by vacuum HTs, which were recently applied also for AM components,^[35–38] but has not been investigated yet for SLM-IN625. HTs under vacuum conditions avoid undesirable effects, such as surface discoloration or oxide layer formation that can occur due to the presence of oxygen. These are particularly unwanted for AM applications where the near net shape components are usually employed with a very limited number of machined surfaces. This work aims to fill these gaps by comparing microstructural, mechanical, and tribological performances of AB SLM-IN625 with different vacuum HTs, which were performed with an industrial furnace so to provide a database of information directly applicable to real parts. The results presented could be especially relevant for a better understanding of material properties and potential failure modes, which are essential to preserve the safety and performance levels required by the critical fields, such as the energy sector, where this superalloy is commonly employed.

Table 1. Chemical composition (wt%) of the commercial IN625-0402 powder.^[34]

In625	Cr	Mo	Fe	Nb	Co	Cu	Mn	Si	Al
20–23	8.0–10	≤5.0	3.15–4.15	≤1.0	≤0.5	≤0.5	≤0.5	≤0.5	≤0.4
	Ti	C	Ta	N	O	P	S	Ni	
	≤0.4	≤0.1	≤0.05	≤0.02	≤0.02	≤0.015	≤0.015	Bal.	

2. Experimental Section

2.1. Samples Description

In this article, commercially available IN625-0402 powder^[39] was used. The nominal composition is reported in **Table 1**. IN625-0402 powder was characterized using scanning electron microscopy (SEM) integrated with energy dispersive X-ray spectrometry for elemental analysis (EDXS). In particular, the morphology and size of the particles were investigated.

Dumbbell specimens, with dimensions of $80 \times 15 \times 3$ mm and a gauge width and length of 5×18 mm, respectively, were produced with IN625-0402 commercial powder by a laser-pulsed SLM Renishaw system in argon atmosphere, according to UNI EN ISO 551-61. The same process was used to produce the wear test samples, which are disk shaped with a diameter of 55 mm and a thickness of 10 mm.

The specimens were built on a stainless-steel base plate along the vertical direction, so that their longitudinal axis was parallel to the tensile load direction, with a layer thickness of 40 μ m, a hatching distance of 110 μ m, laser power of 190 W, point distance (distance between two consecutive points) of 90 μ m, and exposure time (dwelling time of the laser spot at each point) of 100 μ s. The scanning speed can be determined by the ratio between point distance and exposure time, with a value of 900 mm s⁻¹.

SLM is a manufacturing process widely used to produce 3D near-net shape components to reduce productions costs. It is important to highlight that for near-net shaped components with complex geometry it is often impossible to perform a surface finishing treatment due to geometrical constraints. Moreover, these postproduction processes involve additional unwanted costs. For this reason, the mechanical properties were analyzed on sample with AB surface in order to assess the tensile behavior for the general case of SLM components not subsequently machined or subjected to surface postprocessing. The evaluation of mechanical properties with AB surface can also be regarded as a more conservative approach, considering that surface post-processing may help to reduce detrimental effects caused by surface or subsurface defects.

On the contrary, regarding the wear and microhardness tests target values of surface roughness are specifically required by the related standards, and therefore, the samples surface was polished and prepared according to the ASTM G99-17 and ASTM E92-16 standards, respectively.

2.2. HTs

After samples production, the HTs were performed by the company TAV Vacuum Furnaces (Caravaggio (BG), Italy) using a

horizontal furnace for vacuum HT (“TAV H3 all metal”). To avoid any type of contamination and ensure temperature uniformity, all the HTs were carried out under high vacuum (10^{-6} mbar) and the samples were placed on alumina plates. Before each treatment, they underwent a preliminary stage in the oven which consisted in maintaining the samples in high vacuum at room temperature for about 30 min.

In this way, the elimination of all contaminants and gas present both in the chamber and in the specimens was ensured. Successively, each treatment was performed in a vacuum with a partial pressure of argon $P_p = 5$ mbar. This partial pressure is essential to prevent chromium evaporation from the specimens during treatment which would cause a variation in the chemical composition of the alloy and the formation of a golden surface on the samples. Three samples for each condition were analyzed.

To obtain different mechanical behaviors,^[11–13,17–29] the HTs were selected after a careful study of the literature and technical data sheets from manufacturers of SLM technologies, including AB condition (i.e., no treatment) for reference.

Overall, the following conditions were considered: 1) As built (AB)—no HT. 2) Solutioning and ageing (S + A): (a) solutioning treatment: heating from room temperature to 980 °C (heating rate: 10 °C min⁻¹), maintaining at 980 °C for 60 min, and radial cooling from 980 °C to room temperature (furnace cooling rate: 28 °C min⁻¹) with 1.5 bars of Ar. (b) The solubilized samples are maintained at room temperature in a high vacuum for 30 min. (c) Aging treatment: heating from room temperature to 720 °C (heating rate: 10 °C min⁻¹), maintaining at 720 °C for 8 h, and controlled cooling from 720 to 620 °C in 150 min (furnace cooling rate: 0.7 °C min⁻¹). Maintaining at 620 °C for 8 h and radial cooling from 620 °C to room temperature (furnace cooling rate: 17 °C min⁻¹) with 1.5 bars of Ar. 3) Direct ageing (DA): heating from room temperature to 720 °C (heating rate: 10 °C min⁻¹), maintaining at 720 °C for 8 h, and controlled cooling from 720 to 620 °C in 150 min (furnace cooling rate: 0.7 °C min⁻¹). Maintaining at 620 °C for 8 h and radial cooling from 620 °C to room temperature (furnace cooling rate: 17 °C min⁻¹) with 1.5 bars of Ar. 4) Annealing (AN): heating from room temperature to 1150 °C (heating rate: 8 °C min⁻¹), maintaining at 1150 °C for 60 min, and natural cooling performed in furnace from 1150 to room temperature (cooling rate: 5 °C min⁻¹) maintaining the partial pressure $P_p = 5$ bar. 5) Stress relieving (SR): heating from room temperature to 870 °C (heating rate: 10 °C min⁻¹), maintaining at 870 °C for 60 min, and radial cooling from 870 °C to room temperature (furnace cooling rate: 24 °C min⁻¹) with 1.5 bars of Ar.

2.3. Microstructural Observation and Analysis

For metallographic observations, transversal (xy plane) and longitudinal (zx plane) sections of samples for each condition were prepared with standard metallographic techniques (ground with SiC papers and polished with 1 μm diamond paste), in order to evaluate the grade of anisotropy/isotropy. The sections were cut from the shoulders of the tensile specimens prior to the test and etched using Kalling’s reagent (5 g CuCl₂, 100 mL HCl, 100 mL ethanol) for 30–40 s, according to ASTM E407 standard. The

microstructures were investigated using a Leica DMI 5000M optical microscope and LEO EVO-40 XVP scanning electron microscope (SEM) equipped with energy dispersive spectrometers (EDS).

2.4. Hardness and Tensile Test

The influence of post-HT on the mechanical properties, in comparison with AB condition, was investigated through hardness and tensile tests.

Microhardness measurements were carried out along the transversal and longitudinal direction with respect to building axis Z . Vickers microhardness (HV) tests were performed with a Micro Duromat 4000 Reichert Jung instrument, according to ASTM E92-16, using 9.8 N (1 kgf) load applied for 15 s on the polished and etched surfaces used for the microstructural analysis. In particular, the results are presented as average values of at least ten measurements.

The influence of microstructural changes induced by HT was investigated by tensile testing to evaluate Young’s modulus (E), 0.2% yield strength ($\sigma_{p0.2}$), ultimate tensile strength (σ_m), and elongation at failure ($A\%$) in each examined condition. An electromechanical testing machine Instron 3369 equipped with a 50 kN load cell was used with an extensometer for strain measurement (approx. strain rate 0.01 s⁻¹) at a strain rate of 1 mm min⁻¹ and room temperature. Three samples for each condition were tested, following UNI EN ISO 6892-1:2009. Finally, to understand the fracture mode, the tensile fracture surfaces of the samples were also investigated using SEM with a secondary electron (SE) detector.

2.5. Wear Tests

The wear tests were conducted on a THT tribometer pin-on-disc machine with an unlubricated dead weight configuration. The XY surfaces of the samples for wear test were mechanical polished to reach a roughness R_a lower than 0.8 μm, in agreement with ASTM G99 standard. Before wear test the specimens were ultrasonic cleaned with ethylic alcohol. As suggested in the study by Wang et al.,^[30] Si₃N₄ ball of 6 mm in diameter was used as a counterpart.

A normal load of 15 N, a sliding speed of 175 mm s⁻¹, and a total sliding distance of 475 m were applied at room temperature. The diameter of the wear tracks was 10 mm. During the test, the friction coefficient as a function of the sliding distance was recorded. At the end of the test, the wear track 2D and 3D profiles were acquired using the confocal microscope Mitaka PF-60 and specific wear rate W_s defined by the Equation (1) was calculated.

$$W_s = \frac{V}{P \times S} \quad (1)$$

In particular, V is the wear volume expressed in mm³, P is the applied load in N, and S is the total distance covered in m. Five HV1 Vickers hardness measurements were also taken both inside and outside the worn track to investigate the work-hardening as required by ASTM E384 standard. Finally, the wear mechanisms were studied by SEM LEO EVO 40 VPS equipped by EDS probe.

3. Results and Discussion

3.1. Microstructural Observations

The morphology of powders used for the SLM process was analyzed using a SEM LEO EVO-40 XVP showing that most particles exhibit an overall spherical shape, even though some have an irregular morphology and several satellites are present, probably due to the atomization process.^[40] From SEM images, the average powder size was about $25 \pm 9.3 \mu\text{m}$.

The chemical composition of the powder was also verified, confirming the datasheet values for commercial IN625-0402 powder reported in Table 1. The microstructure was analyzed using optical microscopy and SEM microscopy and main observations are reported in the following sections.

3.1.1. Optical Microscopy

Examples of the microstructure for the various conditions under investigation at different magnifications are reported in **Figure 1** and 2 for longitudinal and transverse sections, respectively.

AB: For AB with the optical microscope, at lower magnification, it is possible to note the presence of melt pools evenly distributed and slightly overlapped, as a consequence of the SLM process. In longitudinal sections ("L" in Figure 1), the hemispherical shape of the melt pools is visible with mean dimensions of about $109 \pm 15 \mu\text{m}$ for the width and $53 \pm 12 \mu\text{m}$ for the height. The grains are columnar, with heterogeneous dimensions and elongated in the build direction. Furthermore, at higher magnification, it is possible to note the dendritic structure within the grains. In the transversal section ("T" in Figure 2), typical multifaceted and equiaxed grains are recognizable as austenitic grains. At higher magnification, the presence of precipitates evenly distributed, with local alignments and concentrations,

can also be noticed. These precipitates are probably carbides, given their roundish shape and small size.

S + A: The S + A treatment has limited effects on the microstructure modification. In fact, the solubilization temperature used is too low to cause recrystallization and findings of the present work are in line with literature research,^[12,13,19,28,29] in which it was found that HTs performed at temperatures below 1000°C and for 1 h do not lead to recrystallization. In comparison with AB, the main differences with S + A are the disappearance of dendrites and melt pools in the longitudinal section and the presence of areas formed by small grains in the transversal section. These features could be caused by the recovery phenomenon and the beginning of recrystallization. Anisotropy is still observable in S + A condition with the austenitic grains elongated in the build direction. However, it is important to note that in this condition the grains are less elongated in the build direction respect to AB condition, probably due to the beginning of recrystallization that induced the formation of twinings.^[12,13]

DA: DA is the HT that causes the least microstructure variation compared to the AB condition. Columnar grains and dendritic structures are still visible after DA, which means that this HT has not an important effect on the microstructure, except on anisotropy. The main effect of the DA HT is the precipitation of particles. In this condition, the precipitates are mainly small and with a roundish shape, recognizable as carbides. At higher magnification also, precipitates with different sizes and shapes are visible.

AN: AN is the HT that causes the most apparent changes in the microstructure. A fully recrystallized microstructure is observable in both longitudinal and transversal sections formed by equiaxed grains and twins. Thanks to the recrystallization, isotropy in the microstructure is achieved. The high temperature used for the AN HT leads to partial solubilization of some unintended precipitates and particle coarsening. These phenomena are concomitant with a reduction of yield strength after this

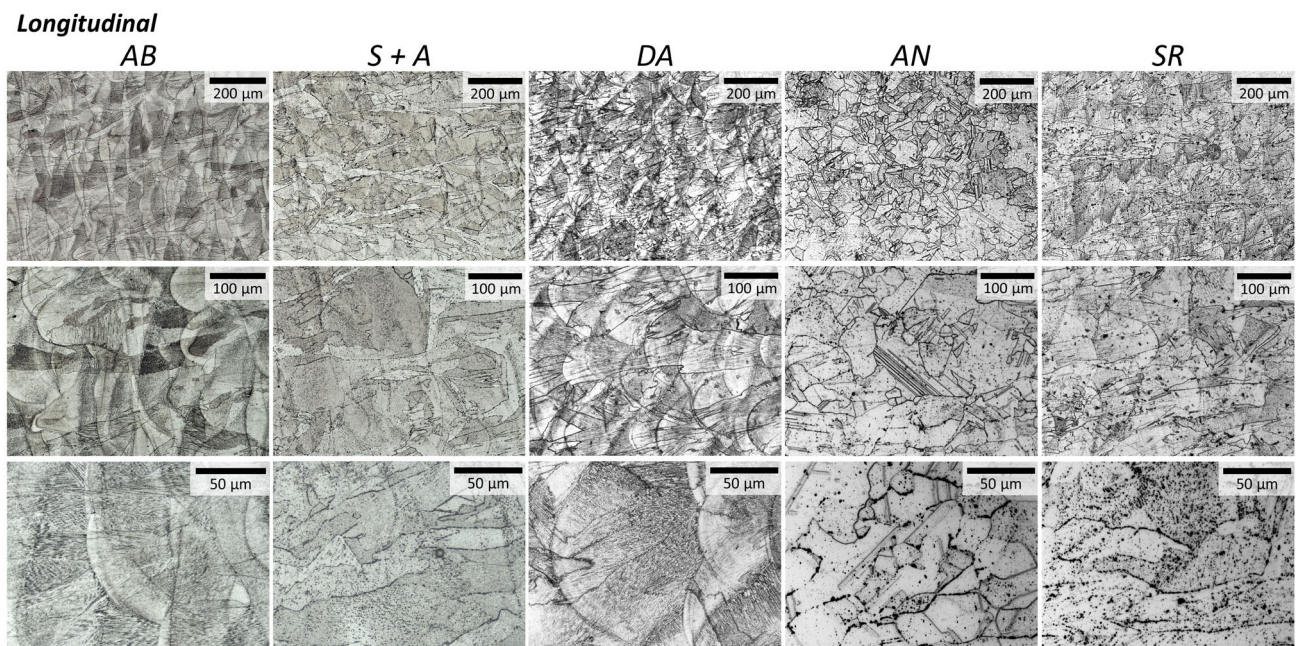


Figure 1. Comparison of microstructure in the longitudinal section at different magnification under different conditions: AB, S + A, DA, AN, and SR.

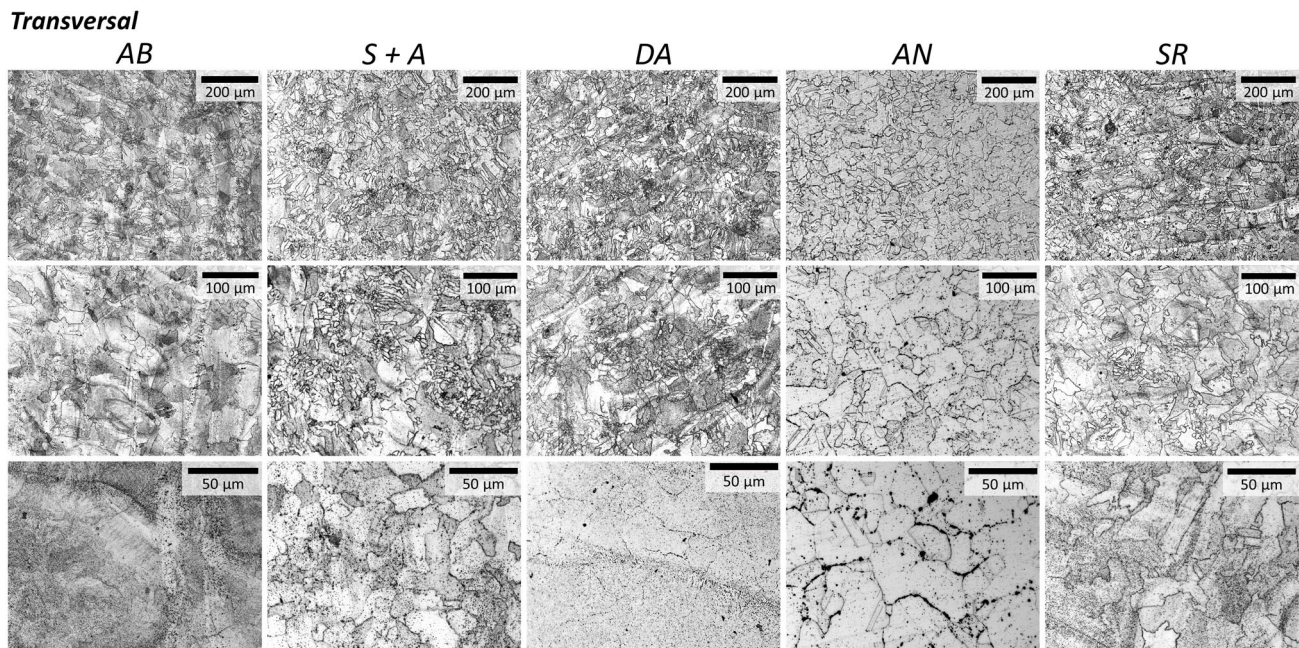


Figure 2. Comparison of microstructure in the transversal section at different magnification under different conditions: AB, S + A, DA, AN, and SR.

HT and these insights seem in line with the results of other researchers. In particular, Li et al.^[18] have observed the formation of carbides during AN at 980 and 1150 °C. Li et al.^[19] reported coarsening of MC carbides from preexisting ones and newly formed carbides at the grain boundaries. Finally, Marchese et al.^[21] studied the effect of HT at 1150 °C for 2 h and have detected with FESEM and TEM analyses the presence of new Nb, Ti-rich MC carbides from 30 to 400 nm.

SR: As shown in Figure 1 and 2, the SR HTs do not affect the microstructure. In fact, it is used only to reduce the residual stress caused by the SLM process and it is not designed to modify the microstructure because the temperature used is low and similar reasoning as S + A applies.

Austenitic grains remain elongated in the build direction as can be seen in Figure 1, whereas in the transversal section grains are equiaxed. If compared to AB condition, grains are smaller, but the anisotropy still remains.

Finally, in **Table 2** the mean grain size and the shape ratio (length (l)/width (w) of the grains) for each condition are reported. As can be seen, there are no particular changes in the grains size, both in each section, both in the different HT conditions. Only for the AN HT it is possible to observe grains size reduction as a consequence of recrystallization. On the contrary, for S + A HT there is a slight growth of the measured grains size in the longitudinal section, due to a modification of the grain's shape. This effect could be a consequence of exposure at a high temperature even though under the recrystallization temperature.^[18]

3.1.2. SEM

SEM integrated with energy dispersive elemental analysis was used to investigate further the microstructure of the samples

Table 2. Mean grain size and Shape ratio (l/w) in the longitudinal (L) and transversal (T) section in different heat treatment conditions to highlight the elongation of the grains.

Mean grains dimension [μm]		Shape ratio (l/w)	
AB—L	AB—T	AB—L	AB—T
58 ± 27	37 ± 5	2.57	0.92
S + A—L	S + A—T	S + A—L	S + A—T
68 ± 31	21 ± 6	1.62	1.07
DA—L	DA—T	DA—L	DA—T
58 ± 18	25 ± 5	1.66	1.22
AN—L	AN—T	AN—L	AN—T
32 ± 16	30 ± 6	1.48	0.95
SR—L	SR—T	SR—L	SR—T
51 ± 16	29 ± 9	1.35	1.29

in longitudinal sections. SEM images and the EDS analysis for AB condition are shown in **Figure 3**. It is important to highlight that C content has been neglected because of the limits of the instrument with light elements. It is possible to note the presence of columnar dendritic structure (highlighted in red) and cellular dendritic structure (highlighted in blue). Semiquantitative chemical analysis obtained by EDS probe confirmed the chemical composition reported in Table 1.

HTs may also influence the type of the precipitates. According to the literature,^[41] block-like precipitates are, in general, rich in Nb (MC carbides) and Mo (M_6C carbides), whereas precipitates shaped as thin film rich in Cr are, in general, $M_{23}C_6$ carbides. Assuming this observation as a guideline, different kinds of

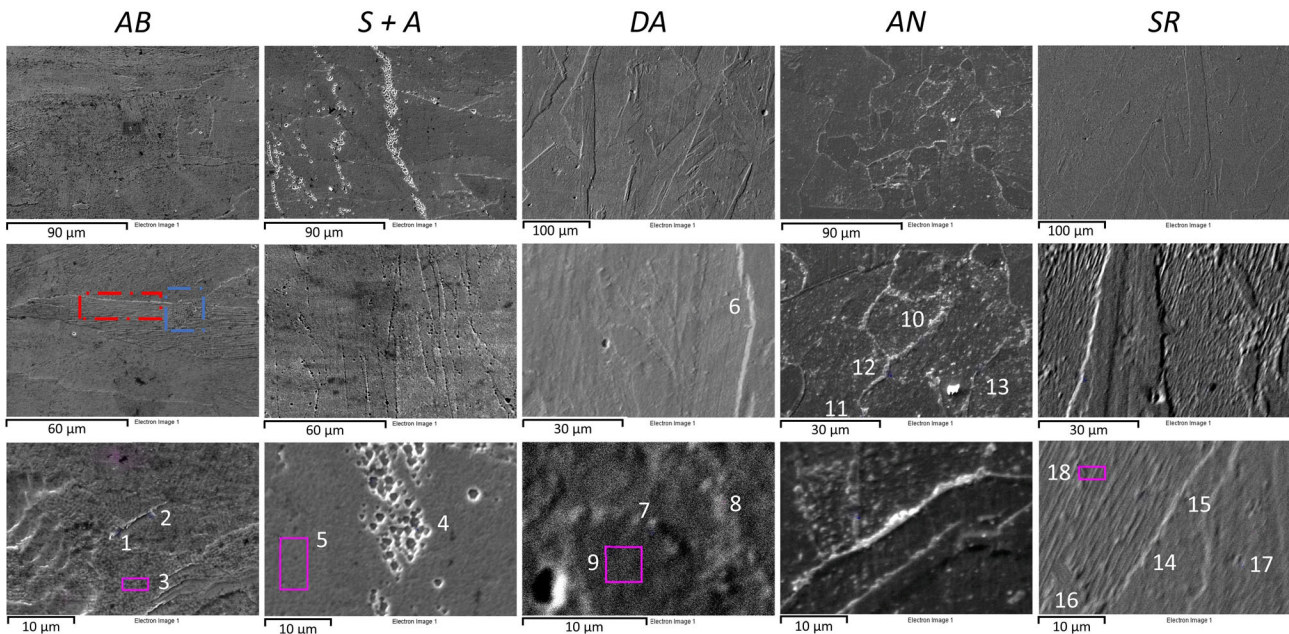


Figure 3. Comparison of SEM images of the longitudinal section at different magnification for each condition.

precipitates were noticed, as highlighted in Figure 3 and summarized in Table 3.

For S + A condition it is possible to note the presence of irregular block-like precipitates, which could be considered M_6C and MC carbides.

Instead for DA condition, both precipitates shaped like a thin film and block-like with high percentages of Nb could be noticed,

Table 3. EDS analysis of SEM images reported in Figure 3.

Samples	Spectrum	Al	Ti	Cr	Fe	Ni	Nb	Mo
AB	1	–	–	23.32	4.36	64.51	–	7.81
	2	0.48	–	22.61	4.39	63.76	–	8.76
	3	–	–	22.94	4.51	64.00	–	8.55
S + A	4	–	–	23.37	4.49	65.57	–	6.57
	5	–	–	23.06	4.56	64.21	–	8.17
DA	6	–	–	25.91	4.31	69.78	–	–
	7	–	–	19.84	4.21	56.30	13.86	5.79
	8	–	–	21.29	3.64	54.17	15.47	5.42
	9	–	–	24.01	4.21	71.79	–	–
AN	10	–	0.15	19.84	3.98	57.95	14.41	3.66
	11	1.48	0.71	21.71	3.83	53.57	14.27	4.43
	12	1.97	0.93	18.30	3.16	55.39	16.99	3.27
	13	–	0.21	20.74	3.96	58.47	12.47	4.14
SR	14	–	–	26.19	–	73.81	–	–
	15	–	–	26.35	3.71	69.94	–	–
	16	–	–	21.71	3.37	54.50	20.42	–
	17	–	0.45	20.14	3.92	54.20	21.28	–
	18	–	–	24.28	5.26	70.46	–	–

which could be interpreted as $M_{23}C_6$, rich in Cr in the former case and as MC carbides in the latter.^[42] It is worthwhile to note that in literature these thin film precipitates could be also identified as δ phase.^[43] This fact is due to the presence of γ'' phase, and carbides, after DA^[21,26]; the δ phase could come from the transformation of γ'' phase which is shaped like thin film. Better investigations (i.e., TEM) need to be done in order to assess the nature of precipitates.

Notably, for the temperatures used in the present work for AN (i.e., 1150 °C) this HT should not lead the formation of precipitate, nevertheless when comparing the microstructure with AB condition precipitates after AN HT were present both inside grains and at the grain boundaries. In particular, block-like precipitates rich in Nb (probably MC carbides) were observed, together with Al and Ti precipitates shaped as elongated film. These could be associated with γ' phase and $M_{23}C_6$ carbides, as a consequence of the following transformation^[43]



However, as no particles are discernible on the small scale, the content of particles seems to be affected by AN. In this research, the precipitates after AN HT at 1150 °C are present both inside grains and at the grain boundaries after a slow cooling.

In the SEM images of SR condition, it is possible to identify different types of precipitates. Film-like precipitates with higher chromium content could be identified as $M_{23}C_6$ carbides, whereas block-like precipitates rich in Nb could again be related to MC carbides. δ Phase was not detected with SEM/EDS, but it is important to highlight that in the literature the formation of δ phase was reported by Stoudt et al.^[23] after the SR HT at 870 °C. This phase has an acicular shape with nanometric size and gives greater hardness and brittleness at the matrix.

As a conclusive remark, it should be pointed out that not only the type, but also the distribution and size of precipitates seem to be affected by the HT parameters, especially the cooling rate. In fact, rapid cooling is used to freeze the solubilized elements in the matrix and suppress the growth of precipitates, whereas a slow cooling promotes the formation and the coarsening of precipitates. Considering SLM-IN625, this aspect has been considered in the work of Zhang et al.^[44] in which the homogenization kinetics of SLM-IN625 was examined. In this case the cooling rate after the AN HT at 1150 °C was very high ($\approx 200\text{ °C min}^{-1}$) in order to freeze the microstructure reporting no carbides at grain boundaries. Also, Marchese et al.^[25] reported only few small precipitates at grain boundaries performing a water quenching after an AN HT at 1150 °C. Instead, considering the case of slow cooling rate, Li et al.^[18] have observed the formation of carbides both in the grains and along the grain boundaries after AN at 980 and 1150 °C followed by a furnace cooling. Also, in the work of Marchese et al.^[21] the effect of HT at 1150 °C for 2 h revealed the presence of fine inter/intragranular Nb, Ti-rich MC carbides from 30 to 400 nm. Finally, Li et al.^[19] reported coarsening of MC carbides from preexisting and newly formed carbides at the grain boundaries after a cooling in still air.

3.2. Vickers Microhardness

The microhardness of the specimens was investigated both along the longitudinal section (ZX plane) and transversal section (XY plane). For the longitudinal section (ZX plane), the average hardness is 296 ± 8 HV, 319 ± 6 HV, 344 ± 6 HV, 221 ± 8 HV, and 296 ± 5 HV, respectively, for AB, S + A, DA, AN, and SR conditions. For the transversal section (XY plane), instead, the average hardness is 291 ± 7 HV, 311 ± 8 HV, 355 ± 9 HV, 216 ± 5 HV, and 301 ± 6 HV, respectively, for AB, S + A, DA, AN, and SR conditions. It should be highlighted that for a conventional forged IN625 a hardness of about 305 HV is reported in the literature,^[19] slightly higher than the present AB condition. As a consequence of aging, HT DA and S + A were able to strongly increase the hardness due to the precipitations of carbides, such as $M_{23}C_6$, MC, and M_6C . S + A sample reached lower values with respect to DA one because of the solution HT that not only solubilizes precipitates and hard phases before the aging treatment, but also can cause a growth in the size of precipitates. This phenomenon is a consequence of the long period at high temperature and can lead to a reduction in hardness. Instead, DA HT allowed the formation of precipitates and phases directly, without changes in the size of precipitates. On the other side, AN caused a significant reduction of the hardness due to the recrystallization phenomenon induced by this treatment. As already mentioned, SR HT is mainly aimed to decrease residual stresses with only minor microstructural effects, as reflected by a hardness value very similar to AB condition.

3.3. Tensile Properties

Figure 4 shows the effects of the HTs on the mechanical properties. In particular, DA HT caused a remarkable increase of the yield strength, tensile strength, and Young's modulus due to the presence of precipitates, i.e., MC, M_6C , $M_{23}C_6$ carbides or δ

phase which, on the other hand, reduced the ductility. It is important to highlight that this trend is confirmed by the highest hardness values of these DA samples, where the δ phase may have played a key role. The opposite situation occurs for AN, in which case the recrystallization results in a relevant increase in the ductility with the highest reduction of the other mechanical properties. S + A is the treatment that offers the best compromise between all the mechanical properties. The combination of solubilization and aging enhances the strength of the samples without reducing the ductility. The solution HT allows a reduction of residual stresses and the recovery's phenomenon, with a beginning of recrystallization, which promotes ductility. Instead, the aging HT DA causes the formation of precipitates that increase the strength of the alloy. Regarding SR condition, this HT does not affect particularly the mechanical properties, except for a slight increase in ductility, possibly thanks to the reduction of residual stresses. In Table 4, a comparison of the mechanical properties is reported, including data from literature for samples obtained by traditional processes (such as forging, rolling, and casting) and by SLM. The values obtained in this article for the AB condition are well above the minimum values required by reference standard ASTM B443 for SLM samples. Besides, AB conditions show similar properties with rolled and forged conditions, but higher than as-cast samples. Forging and rolling processes can induce strain hardening in the alloy, which allows to obtain high values of yield strength ($\sigma_{p0.2}$) and ultimate tensile strength (σ_R). On the contrary, SLM is not designed to induce strain hardening, but the elevated cooling rate reached with this process causes the formation of a very fine dendritic structure in the built direction. This feature gives strength to the alloy.

3.4. Fracture Surfaces Analysis

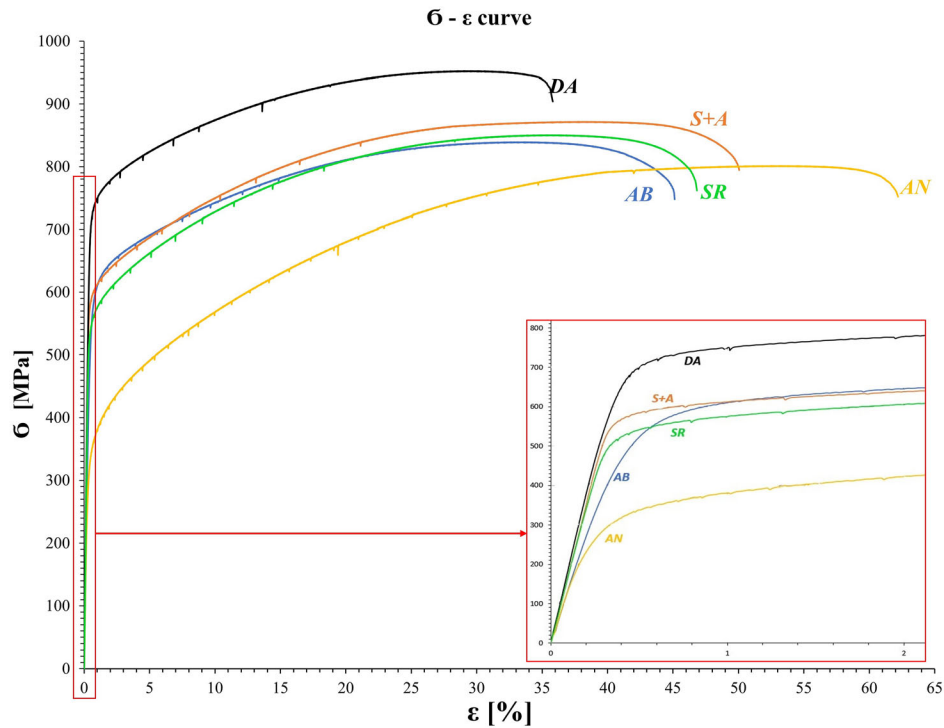
Fracture surfaces were observed using SEM to investigate the fracture's mechanisms and some representative fractographies are reported in Figure 5.

At a first visual inspection, all the broken samples showed necking and jagged surfaces which suggest ductile fracture mode. In the overview of AB sample (Figure 5), it is possible to see the presence of a central area with a relevant ductile aspect delimited by an upper and lower area morphologically flat, probably caused by the final failure. Very small dimples are clearly visible, which indicate ductile fracture mode, as well as cavities with different sizes and lack of fusion defects (highlighted by a blue arrow).

S + A sample shows a flatter surface than AB condition with local alignments of cavities which are well shown at higher magnifications. Red arrows highlight microcracks at 45° which link voids. In this condition, very fine and evenly distributed dimples are also visible, again suggesting that ductile fracture mode occurred.

The fracture surface in DA samples is clearly ductile, but with a lower extension of the area deformed during the tensile test (upper half of the surface). At higher magnifications, voids, microcracks, and dimples are visible in line with a ductile behavior.

Different behavior can be noticed for AN samples. In the overview, only a small portion at the lower area of the fracture surface



	AB		S+A		DA		AN		SR	
	Avg.	Std. Dev.	Avg.	Std. Dev.	Avg.	Std. Dev.	Avg.	Std. Dev.	Avg.	Std. Dev.
$\sigma_{p0.2}$ [MPa]	554	3	578	4	711	8	339	15	543	1
σ_R [MPa]	839	1	866	8	955	4	800	1	851	1
A% [%]	45.3	0.3	47.2	3.3	36.5	1.0	61.3	1.3	46.1	1.1
E [GPa]	131	9	187	18	182	11	159	32	172	1

Figure 4. Stress–strain curve for the different heat treatment conditions.

Table 4. Comparison of mechanical properties of samples obtained by SLM and traditional processes.

Conditions	$\sigma_{p0.2}$ [MPa]	σ_R [MPa]	A% [%]
AB SLM	554	839	45.3
Standard SLM ^[11]	275	485	30
Rolled ^[1]	414–758	827–1103	60–30
Forged ^[36]	490	965	50
As-cast ^[36]	350	710	48

is flat, which is associated with the final rupture, whereas the large extent of a rough surface indicates a more ductile sample. Voids and microcracks are visible also in this condition with very fine and evenly distributed dimples similarly to S + A.

The fracture surface of the last condition (SR) is very similar to the other ones analyzed. The flat area in the upper half of the surface probably indicates the final rupture of the sample, whereas the remaining surface was deformed during tensile test. Some voids are highlighted by yellow arrows and very fine dimples are clearly visible.

3.5. Wear Tracks Investigation

Figure 6 and 7 show the wear track morphologies after the test. The shapes of all the tracks are, in general, regular and the width is quite constant along the track. Only DA condition is different with an irregular shape and width along the track, which is also smaller with respect to the other conditions. For a better comprehension of the morphology of the tracks, Figure 6 is reported. In Figure 6 which shows a 3D image of the wear track, the presence of grooves in all conditions as a consequence of the abrasive wear mechanism is clearly visible. The deposition of material on the surface to form relief plates is responsible for the dark areas on it. They can be caused either by debris not properly evacuated from the track or by the formation of oxides. No delamination is visible for any of the examined conditions. The wear tracks are very similar in terms of shape, width, and depth except for the DA sample, as can be seen in Figure 6 and Table 5. In fact, the depth and the width of the wear track in the DA condition are, respectively, about 60% and 27% lower than the other conditions. This difference can also be appreciated for the specific wear rate W_s data reported in Table 5, where the DA sample shows a value much lower than the other conditions (about 72% lower).

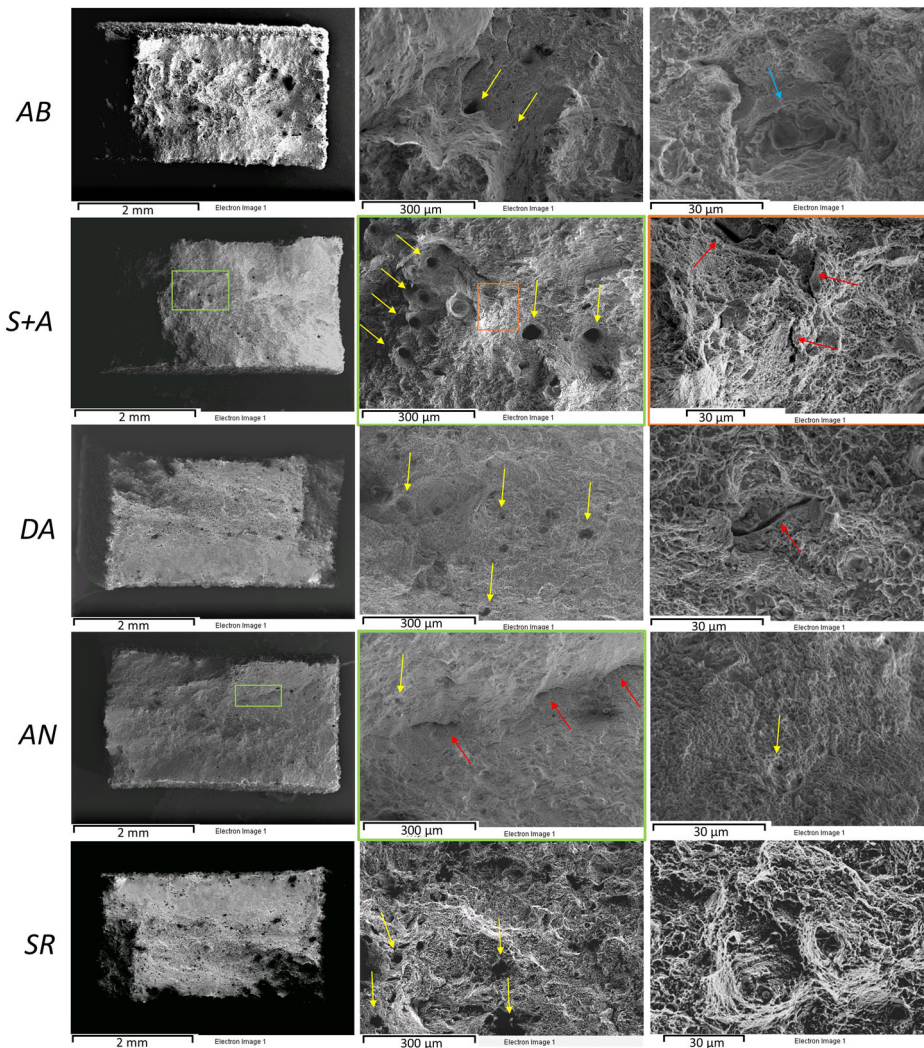


Figure 5. Surface fracture images obtained by SEM for the different heat treatment conditions. Yellow arrows indicate holes, red arrows indicate micro-cracks, and blue arrows indicate lack of fusion.

The beneficial effects of the precipitations of carbides as a consequence of aging treatment are perceptible also for the S + A condition. The wear rate for this condition is 15% lower than the AB condition. AN and SR HT show higher values of wear rate, respectively, 3.5% and 11.5% more than the AB condition. The reasons are linked to the fact that these treatments do not cause a strengthening in the matrix, as can be seen in hardness and mechanical properties. The different behavior of the DA condition is reflected also in the coefficient of friction (COF), both considering the stabilized value (Table 5) and the trend during the test (Figure 8). In particular, all the samples showed similar behavior in terms of COF, with the notable exception of the DA condition that exhibited a lower COF (about 68% lower).

In addition, the trend of COF during the wear test in the DA condition seems similar to the other samples at the beginning of the test but successively showed a drastic and instantaneous reduction at about 20% of the test time. After this, COF decreased slowly until the end of the test. For a comparison

purpose, Wang et al.^[30] studied the wear behavior of hot extruded IN625 and, in the same test condition of this work, it was found a mean COF value of 0.7, so 25% higher than SLM IN625 in AB condition. For a better comprehension of the different behavior of the DA condition, a SEM analysis was carried out. Figure 9 and Table 6 show SEM images and EDS analyses for the different conditions. As seen above, grooves and deposition of material in internal and external parts of the tracks are visible. In particular, in the backscattered images of all the conditions it is possible to note two types of deposited material: oxides of material from counterpart pin (dark grey) and debris from base metal (light grey). The former is highlighted by the presence of oxygen and silicon that come from the pin, the latter by the chemical composition similar to the base metal.

Taking into account the results analyzed above, the reason why the DA sample has such different behavior can be related to the high hardness of this condition. First, the higher is the hardness and the lower is the amount of material that can be removed. The

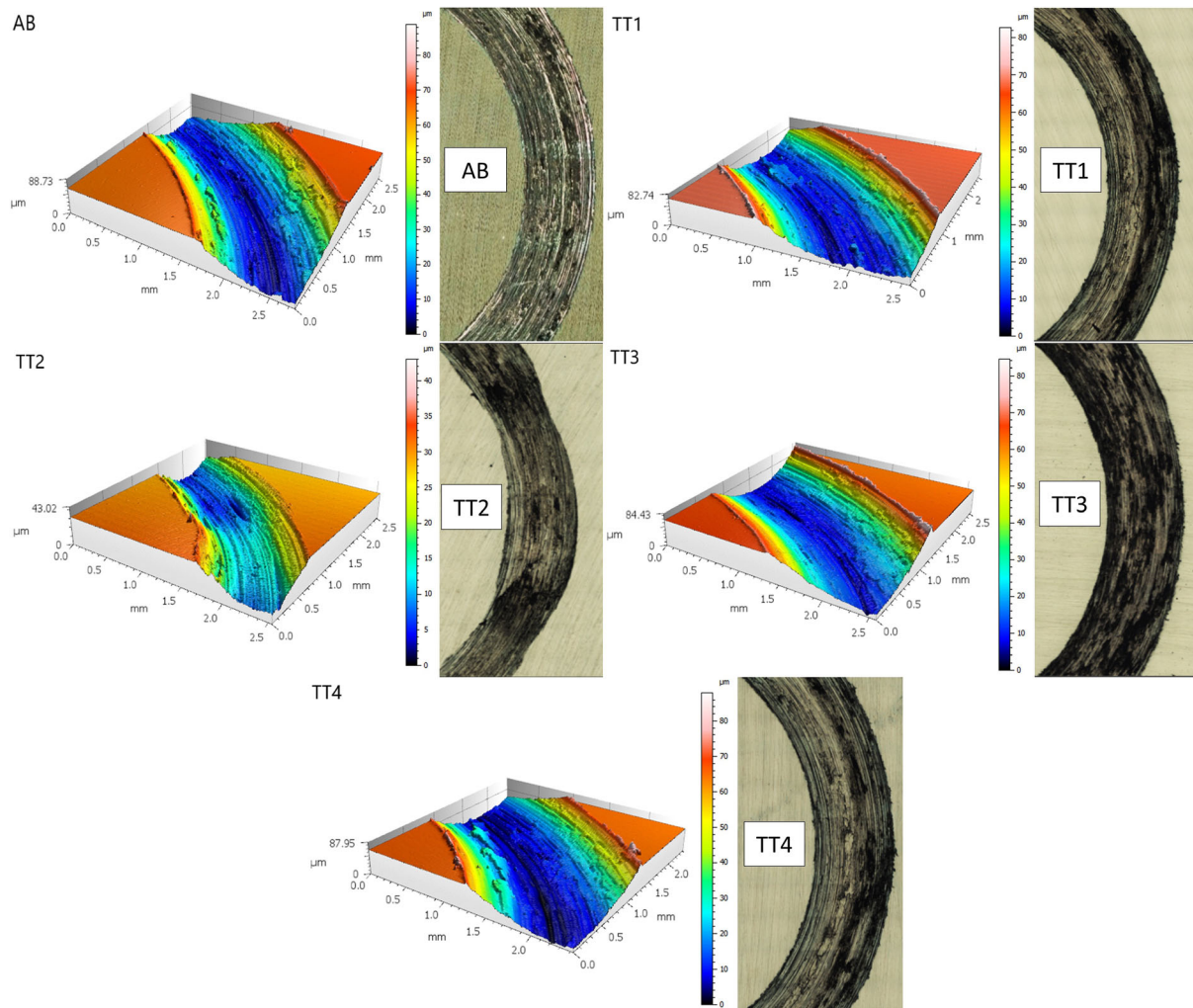


Figure 6. Portion of the wear track under different heat treatment conditions observed by confocal microscope.

high hardness is caused by the HT which allows the formation of a significant number of precipitates (mainly MC and $M_{23}C_6$ carbides). Second, hardness allows the formation of a stable oxides layer on the wear track, thanks to the high resistance of the base metal. This harder layer allows protection from the wear mechanism, reducing the COF, the wear volume, and consequently the specific wear rate and the dimension of the wear track. In the other conditions, the hardness is not high enough to prevent the collapse of the oxide layer causing its fragmentation. This situation reduces the protection of the base metal from wear and can explain why all the other conditions have instead a similar behavior.

4. Conclusions

In this work, the effects of different vacuum HTs on microstructure and on mechanical and tribological behaviors of SLM IN625 were investigated. The HTs performed on specimens were S + A, DA, AN, and SR.

The data obtained by the tests were discussed to give an exhaustive explanation of the IN625 response to vacuum HTs. Conclusions can be summarized as follows: 1) The microstructure obtained in the different conditions is the results of the entire thermal history including the SLM process and the HTs with their slow cooling. The AB microstructure is formed by columnar grains which grow in the build direction. Within the grains, a very fine dendritic structure is present. As a consequence of the SLM process, evenly distributed and slightly overlapped melt pools are formed. Solution and aging HT allowed the elimination of the melt pools and the formation of precipitates in the matrix. DA HTs did not alter the microstructure but caused extensive and uniform precipitation of carbides and secondary phases. SEM–EDS analysis revealed that the main precipitates seem to be $M_{23}C_6$ and MC carbides, as well as γ'' and δ phases. AN is the HT that more has modified the microstructure due to the recrystallization phenomenon. For this reason, an equiaxed and almost isotropic microstructure was obtained. SR did not change in a significant way the microstructure. 2) Mechanical properties are strictly correlated to microstructural

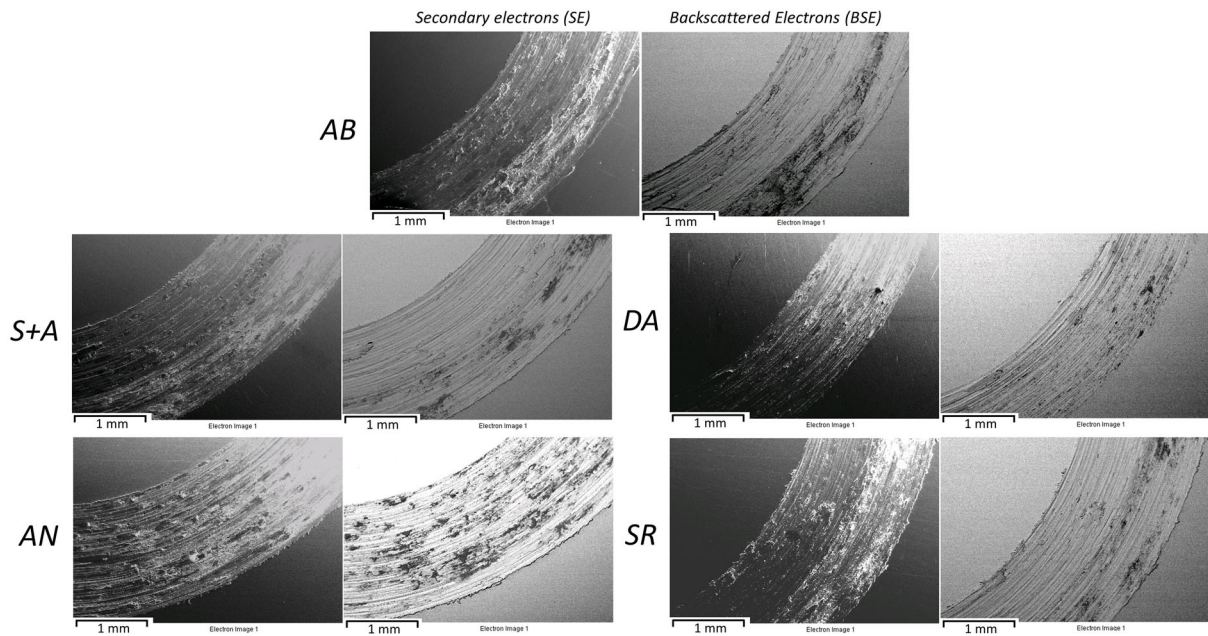


Figure 7. Portion of the wear track under different heat treatment conditions observed by SEM.

Table 5. Average Depth and width of the wear tracks, specific wear rate and average coefficient of friction for the different conditions.

	AB		S + A		DA		AN		SR	
	Avg.	Std. dev.	Avg.	Std. dev.	Avg.	Std. dev.	Avg.	Std. dev.	Avg.	Std. dev.
Depth of wear track [μm]	68.3	0.9	69	1.4	28	2.2	68.7	0.8	70.8	2.7
Width of wear track [μm]	1715.1	26.9	1785.4	18.7	1284.1	69.7	1771.6	10.3	1781.6	27.5
Specific wear rate [$10^{-3} \text{ mm}^3 (\text{N m})^{-1}$]	0.313	0.027	0.352	0.010	0.087	0.009	0.323	0.012	0.349	0.022
COF μ	0.566	–	0.562	–	0.183	–	0.565	–	0.565	–

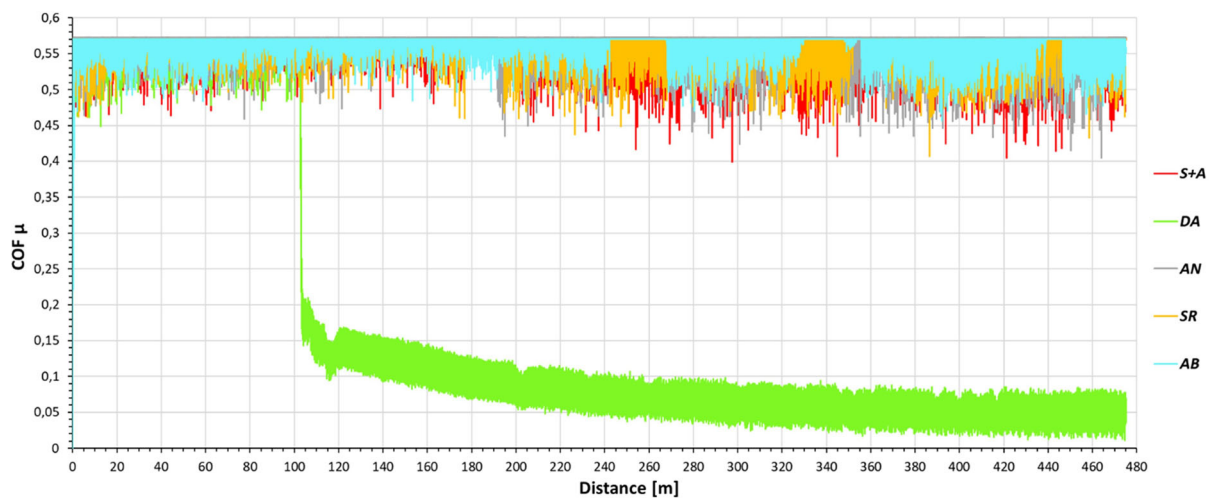


Figure 8. Trend of COF during the wear test for the different conditions.

modifications. Compared to AB condition, only SA and DA HTs have achieved higher strength ($\sigma_{p0,2}$ and σ_R) thanks to the formation of precipitates which act as obstacles to the dislocations'

movement. In the case of SA, the increase in strength is lower than DA, but it did not reduce the ductility as DA condition. AN HT led to a strong increase in ductility thanks to the

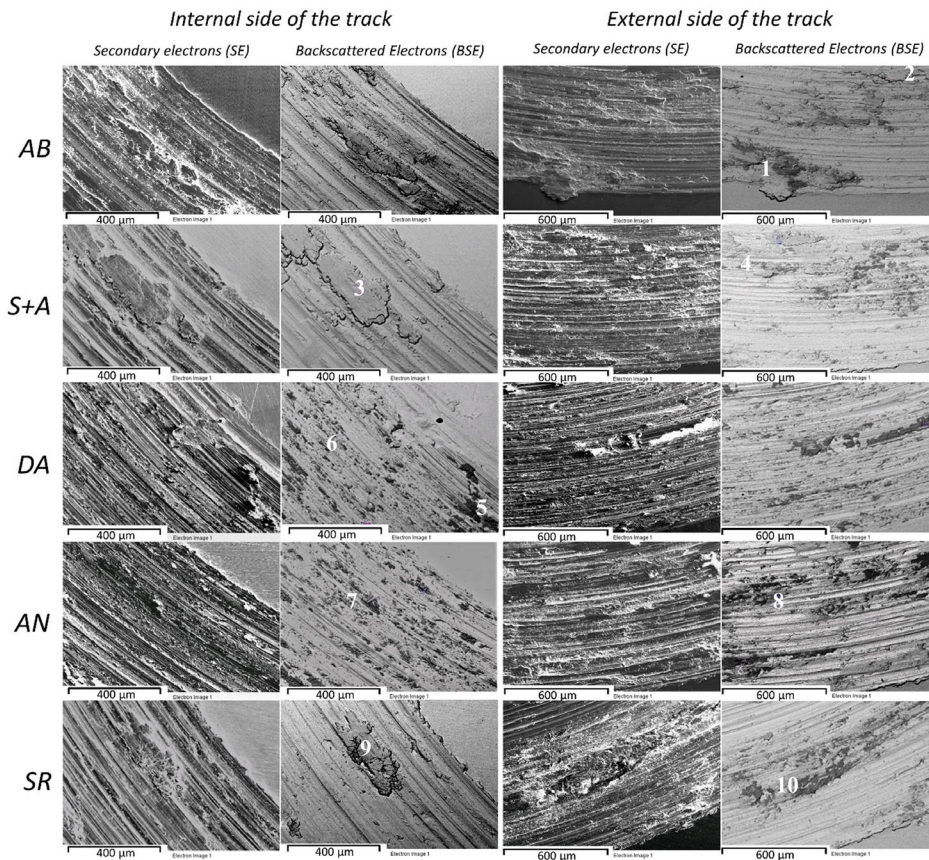


Figure 9. SEM images of internal and external side of the wear tracks for the different conditions.

Table 6. EDS analysis of SEM images reported in Figure 9.

Samples	Spectrum	O	Si	Cr	Fe	Ni	Mo
AB	1	19.08	0.68	19.25	3.61	50.89	6.49
	2	5.49	–	22.46	4.21	59.54	8.29
S + A	3	4.71	–	22.28	4.35	61.32	7.34
	4	25.06	1.81	17.17	3.25	46.62	6.09
DA	5	25.24	0.73	17.00	3.27	47.38	6.38
	6	20.38	–	18.67	3.49	50.12	7.35
AN	7	30.1	2.41	16.13	2.81	43.15	5.41
	8	18.72	0.67	19.45	3.44	51.75	5.97
SR	9	4.36	–	22.35	4.45	60.85	7.99
	10	27.00	1.47	16.98	2.96	45.36	6.23

recrystallization phenomenon, which, on the other hand, has reduced a lot the strength of the alloy. SR did not alter significantly the mechanical properties compared to AB condition. 3) Fracture surface analysis revealed that all the conditions underwent ductile fracture mode of failure. The DA condition has shown a plastic deformed area less extended than the other conditions, a sign of less ductility. 4) Vickers microhardness values are in accordance with what was observed for microstructure and mechanical properties. In particular, DA condition reached

the higher value of hardness thanks to the presence of evenly distributed carbides in the matrix. Also, S + A HT allowed an increase in hardness, but less than the previous condition. As expected, AN condition has reported low values of Vickers microhardness as a consequence of recrystallization. SR did not significantly affect the microhardness, showing values similar to AB condition. 5) Wear behavior was not appreciably affected by the HTs, except for DA HTs. All the conditions analyzed led to very similar values of COF, wear rate, and morphology of the wear tracks. DA condition performed much better than other conditions with very low values of COF, wear rate, and sizes of wear track. This behavior could be linked to the fact that DA HTs caused extensive precipitation of very fine carbides which hardened the matrix. For this reason, the matrix could properly support the oxides layer formed during the wear test without cause it to collapse. At this point, the oxides layer could protect the matrix from wear. In the other conditions the hardness is not high enough to prevent the collapse of the oxide layer causing its fragmentation. In the different conditions analyzed, abrasive and tribo-oxidative wear mechanisms occurred.

IN625 superalloy obtained by SLM process can reach the mechanical properties obtained by traditional processes with great advantages on the design. In addition, the use of HTs can be a powerful tool to significantly change the mechanical properties and the microstructure to satisfy different requirements.

Acknowledgements

The authors would like to express their gratitude for cooperation to RENISHAW S.p.A., in particular to Ing. Enrico Orsi and Ing. Andrea Penna, for the production of the samples, to TAV VACUUM FURNACES S.p.A., especially to Ing. Alessandro Fiorese and Ing. Andrea Gionda, for the execution of heat treatments, and to Ing. Gabriele Allegri for performing analyses with confocal microscope.

Open Access Funding provided by Università degli Studi di Brescia within the CRUI-CARE Agreement.

Conflict of Interest

The authors declare no conflict of interest.

Data Availability Statement

Research data are not shared.

Keywords

625 Inconel alloy, heat treatments, mechanical properties, selective laser melting, wear

Received: July 28, 2021

Revised: November 16, 2021

Published online:

- [1] Special Metals Company, *INCONEL® Alloy 625 data sheet*, www.specialmetals.com (accessed: May 2021).
- [2] M. Leary, M. Mazur, H. Williams, E. Yang, A. Alghamdi, B. Lozanovski, X. Zhang, D. Shidid, L. Farahbod-Sternahl, G. Witt, I. Kelbassa, P. Choong, M. Qian, M. Brandt, *Mater. Des.* **2018**, 157, 179.
- [3] D. Ulutan, T. Ozel, *Int. J. Mach. Tool. Manu.* **2011**, 51, 250.
- [4] I. Koutiri, E. Pessard, P. Peyre, O. Amlou, T. De Terris, *J. Mater. Process. Technol.* **2018**, 255, 536.
- [5] B. Song, X. Zhao, S. Li, C. Han, Q. Wei, S. Wen, J. Liu, Y. Shi, *Front. Mech. Eng.* **2015**, 10, 111.
- [6] Z. Alomar, F. Concli, *Adv. Eng. Mater.* **2020**, 22, 2000611.
- [7] G. Marchese, X. Garmendia Colera, F. Calignano, M. Lorusso, S. Biamino, P. Minetola, D. Manfredi, *Adv. Eng. Mater.* **2017**, 19, 1600635.
- [8] I. Yadroitsev, L. Thivillon, Ph. Bertrand, I. Smurov, *Appl. Surf. Sci.* **2007**, 254, 980.
- [9] C. Pleass, S. Jothi, *Addit. Manuf.* **2018**, 24, 419.
- [10] A. Md Ashabul, *Doctoral Dissertation, University of Louisville*, **2018**.
- [11] S. Tremamunno, *Master Thesis, Politecnico di Torino*, **2018**.
- [12] G. Marchese, S. Parizia, M. Rashidi, A. Saboori, D. Manfredi, D. Ugues, M. Lombardi, E. Hryha, S. Biamino, *Mater. Sci. Eng., A* **2020**, 769, 138500.
- [13] L. Qin, C. Che, M. Zhang, K. Yan, G. Cheng, H. Jing, X. Wang, *Rapid Prototyp. J.* **2017**, 23, 1119.
- [14] L. Li, F. Liou, *Metals* **2021**, 11, 1003.
- [15] Y. L. Hu, Y. L. Li, S. Y. Zhang, X. Lin, Z. H. Wang, W. D. Huang, *Mater. Sci. Eng. A* **2020**, 772, 138711.
- [16] T. Antonsson, H. Fredriksson, *Metall. Mater. Trans. B* **2005**, 36, 85.
- [17] J. Nguejio, F. Szmytka, S. Hallais, A. Tanguy, S. Nardone, M. Godino Martinez, *Mater. Sci. Eng. A* **2019**, 764, 138214.
- [18] C. Li, R. White, X. Y. Fang, M. Weaver, Y. B. Guo, *Mater. Sci. Eng. A* **2017**, 705, 20.
- [19] S. Li, Q. Wei, Y. Shi, Z. Zhu, D. Zhang, *J. Mater. Sci. Technol.* **2015**, 31, 946.
- [20] F. Xu, Y. Lv, Y. Liu, B. Xu, P. He, *Phys. Procedia* **2013**, 50, 48.
- [21] G. Marchese, M. Lorusso, S. Parizia, S. Parizia, E. Bassini, J.-W. Lee, F. Calignano, D. Manfredi, M. Terner, H. Hong, D. Ugues, M. Lombardi, S. Biamino, *Mater. Sci. Eng., A* **2018**, 729, 64.
- [22] M. Beretta, *Master Thesis, Politecnico di Torino*, **2020**.
- [23] M. R. Stoudt, E. A. Lass, D. S. Ng, M. E. Williams, F. Zhang, C. E. Campbell, G. Lindwall, L. E. Levine, *Metall. Mater. Trans. A* **2018**, 49, 3028.
- [24] X. Xing, X. Di, B. Wang, *J. Alloy Compd.* **2014**, 593, 110.
- [25] G. Marchese, E. Bassini, M. Calandri, E. P. Ambrosio, F. Calignano, M. Lorusso, D. Manfredi, M. Pavese, S. Biamino, P. Fino, *Met. Powder Rep.* **2016**, 71, 273.
- [26] A. Kreitzberg, V. Brailovski, S. Turenne, *Mater. Sci. Eng., A* **2017**, 700, 540.
- [27] M. G. Burke, W. J. Mills, R. Bajaj, *presented at Superalloys*, The University of Manchester, January 2001.
- [28] K. Inaekyan, A. Kreitzberg, S. Turenne, V. Brailovski, *Mater. Sci. Eng., A* **2019**, 768, 138481.
- [29] A. Kreitzber, V. Brailovski, S. Turenne, *Mater. Sci. Eng., A* **2017**, 689, 1.
- [30] Y. Wang, Z. Sixiang, J. Zhi, J. Jinjin, L. Dexue, G. Tingbiao, D. Yutian, *Adv. Mater. Sci. Eng.* **2020**, 2020, 1.
- [31] P. Deng, Y. Chengwu, F. Kai, H. Xiangxiang, L. ZhuGuo, L. Yuyan, Z. Haixing, *Surf. Coat. Tech.* **2017**, 335, 334.
- [32] K. Feng, Y. Chen, D. Pingshun, L. Yuyan, Z. Haixing, L. Fenggui, L. Ruifeng, H. Jian, L. ZhuGuo, *J. Mater. Process. Technol.* **2017**, 243, 82.
- [33] E. Tascioglu, Y. Kaynak, Ö. Poyraz, A. Orhangül, S. Ören, in *Advanced Surface Enhancement, INCASE 2019, Lecture Notes in Mechanical Engineering* (Eds.: S. Itoh, S. Shukla), Springer, Singapore, **2020**, pp. 263–272.
- [34] G. Yong, M. Zhou, *Appl. Sci.* **2018**, 8, 2439.
- [35] D. Sangid, T. A. Book, D. Naragani, J. Rotella, P. Ravi, A. Finch, P. Kenesei, J. S. Park, H. Sharma, J. Almer, X. Xiao, *Addit. Manuf.* **2018**, 22, 479.
- [36] G. Nicoletto, S. Maisano, M. Antolotti, F. Dall'Aglio, *Proc. Struct. Integrity* **2017**, 7, 133.
- [37] S. Ghouse, R. N. Oosterbeek, A. T. Mehmood, F. Vecchiato, D. Dye, J. R. T. Jeffers, *Addit. Manuf.* **2021**, 47, 102262.
- [38] M. J. Bermingham, L. Nicastro, D. Kent, M. S. Dargusch, *J. Alloys Compd.* **2018**, 753, 247.
- [39] Renishaw plc., *Data Sheet: In625-0402 Powder for Additive Manufacturing*, <https://www.renishaw.com/en/data-sheets-additive-manufacturing--17862> (accessed: May 2021).
- [40] S. Singh, S. Ramakrishna, R. Singh, *J. Manuf. Process.* **2017**, 25, 185.
- [41] M. J. Donachie, S. J. Donachie, *Superalloys: A Technical Guide*, 2nd ed., ASM International, Materials Park, OH **2002**.
- [42] F. Marinucci, *Master thesis, Politecnico di Torino*, **2018**.
- [43] F. Zhang, J. Ilavsky, G. Lindwall, M. R. Stoudt, L. E. Levine, A. J. Allen, *Appl. Sci.* **2021**, 11, 8643.
- [44] F. Zhang, L. Levine, A. Allen, C. Campbell, E. Lass, C. Sudha, M. Stoudt, M. Williams, Y. Idell, *Scr. Mater.* **2017**, 131, 98.